

Improved electro-assisted removal of phosphates and nitrates using mesoporous carbon aerogels with controlled porosity

C. Macías · P. Lavela · G. Rasines ·
M. C. Zafra · J. L. Tirado · C. O. Ania

Received: 10 March 2014 / Accepted: 9 June 2014 / Published online: 6 July 2014
© Springer Science+Business Media Dordrecht 2014

Abstract Three-activated carbon aerogels were synthesized by CO₂ activation of the materials prepared by the polycondensation of resorcinol and formaldehyde mixtures followed by supercritical drying. The obtained carbon aerogels were characterized and used as electrode materials for the electrosorption of sodium phosphate and nitrate. X-ray diffraction and Raman spectroscopy showed the dependence of the structural ordering of the aerogels with the resorcinol/catalyst ratio and the extent of activation. The electrosorption capacitance evaluated by cyclic voltammetry revealed large values for the activated samples containing a large contribution of mesopores, regardless the electrolyte salt. Due to an adequate combination of chemical and porous features, the desalting capacity of the activated carbon aerogel electrodes exceeded that of the as-prepared materials. The evaluation of the kinetic properties by chronocoulometric relaxation and impedance spectroscopy showed a decrease of time constant and resistances for highly mesoporous activated samples. A high deionization capacity and fast electrode discharge was detected for the deionization of sodium nitrate on the highly

mesoporous activated aerogel. Data also showed the efficient electrosorption of ionic species on consecutive charge/discharge cycles, confirming the stability of the aerogel electrodes at the high applied potentials.

Keywords Carbon aerogel · Electrosorption · Voltammetry · Impedance spectroscopy

1 Introduction

Much attention has been paid on structurally disordered carbons as materials with interesting properties for energy storage and environmental applications [1–3]. Their suitable electrical and thermal conductivity, adequate corrosion resistance, low thermal expansion coefficients, low densities, and low elasticity make them outstanding materials that can be produced at low cost and high purities for technological uses. High porosity can be achieved by selecting appropriate synthesis routes which allow controlling the microstructure at the nanometer scale. Also, activation processes can be applied to increase the pore volumes and adjust the pore size distribution, with porosity values easily exceeding 80 % and surface areas as high as 2,000 m² g⁻¹. Most commonly, activation processes consist of a partial burn-off of the amorphous carbon under mild oxidation conditions. For this purpose, various procedures including physical activation using CO₂ or steam and chemical activation with hydroxides and carbonates are usually performed [4]. These highly porous carbons are especially interesting for their use as electrodes in electrosorption processes [5, 6].

When a voltage is applied between two porous carbon electrodes immersed in an inert electrolyte, an electrical double layer is formed at the interface of each electrode.

Electronic supplementary material The online version of this article (doi:10.1007/s10800-014-0705-z) contains supplementary material, which is available to authorized users.

C. Macías · G. Rasines
Nanoquímica S.L, PCT Rabanales 21, Ed. Aldebarán M.4.7,
14014 Córdoba, Spain

P. Lavela (✉) · M. C. Zafra · J. L. Tirado
Laboratorio de Química Inorgánica, Universidad de Córdoba,
Marie Curie, Campus de Rabanales, 14071 Córdoba, Spain
e-mail: iqlacarp@uco.es

C. O. Ania
Instituto Nacional del Carbón (INCAR, CSIC), Apartado 73,
33080, Oviedo, Spain

The electro-assisted removal of ionic compounds is based on the separation of the charged species at the electrode/electrolyte interface due to electrostatic interactions. Thus, the charged species in the solution move to and are held on the opposite-charged electrode surface. The electro-adsorption/desorption cycles are highly reversible due to the electrostatic nature of the interactions existing between the electrodes and the electrolytic solution. Based on this mechanism, large surface area electrodes are required for achieving high desalting capacities. Pore size is also important since the adsorption of large solvated ions into small pores could be considered as a limitation of the deionization process [7]. Otherwise, the concept of an electric double layer formed by solvated ions adsorbed on sub-nanometer size pores cannot be strictly applied [8, 9].

Although studies on the electrosorption of ions were initiated several decades ago, advances on this technology have remained somewhat behind due to the lack of adequate electrode materials. For their versatility of forms and structures, a large number of carbon materials are currently being researched to optimize their electroadsorptive properties, including carbon fibers and nanotubes [10, 11], carbon cloths [12], carbide-derived carbons [13], graphene [14], activated carbons [15], carbon aerogels [16], and templated carbon [17]. Besides, hierarchical porous carbon has also been evaluated as promising materials for capacitive deionization [18, 19]. Due to a unique combination of physicochemical and structural properties, that may be conveniently adapted during the synthesis and processing, carbon aerogels possess great potential and versatility as electrodes in electrochemical applications [20, 21]. Carbon aerogels are particularly interesting electrode materials as the supercritical drying leads to a better preservation of the pore structure of the polymerized gel, due to the lack of interfacial tensions during drying.

The objective of this work was to investigate the electrochemical behavior of micro/mesoporous activated carbon aerogels prepared using different resorcinol/catalyst ratios as electrodes for the removal of ions (i.e., phosphates and nitrates). The desalting capacity of the activated aerogels has been compared to that of the aerogels prepared from the polycondensation of resorcinol and formaldehyde. The structural and morphological properties of the electrode materials have been characterized and the capacitive behavior has been determined by voltammetric and impedance analysis. Phosphates and nitrates are ionic species included in fertilizers, thus posing a great long-term environmental impact to groundwater pollution due to agricultural activities [22]. Although many studies report the electrosorption of ions in carbon electrodes, including aerogels, scarce studies focus on the electro-assisted removal of these anions [23].

2 Experimental section

2.1 Materials preparation

Three carbon aerogels were synthesized by the sol–gel polymerization method reported by Pekala [24]. Resorcinol (R) and formaldehyde (F) were dissolved in water (W), and sodium carbonate was added as a catalyst (C). Three resorcinol/catalyst (R/C) ratios were fixed (i.e., 200, 400 and 600) in order to obtain aerogels with different porous structures. Otherwise, the R/F molar ratio was set at 0.5, and the R/W at 0.06. The precursors were mixed in sealed glass moulds under magnetic stirring and allowed to undergo gelation and aging in an oven at 40 °C for 24 h and 70 °C for 120 h. Subsequently a controlled water–acetone exchange was carried out, and then the samples were dried under CO₂ supercritical conditions. Finally, the aerogels were pyrolysed at 800 °C under nitrogen atmosphere with a controlled heating program (i.e., heating rate 2 °C min^{−1} up to 400 °C and hold for 60 min followed by heating up to 800 °C and hold for 60 min) [25]. For the sake of clarity, the pyrolyzed samples will be named as CAGXP, where X is the corresponding R/C value. A second batch of samples was prepared by activation under a CO₂ stream at 800 °C for 2 h. These samples will be named as CAGXA.

2.2 Structural and textural characterization

X-Ray diffraction (XRD) patterns were recorded with a Siemens D500 diffractometer furnished with Cu K α radiation and a graphite monochromator. The baseline was corrected and the Lorentz and polarization factor was applied before the determination of the line width and the position of the reflections. The pore structure of the carbon aerogels was characterized by N₂ adsorption–desorption isotherms at −196 °C (ASAP 2010, Micromeritics). The carbon aerogels were previously outgassed under primary vacuum at 120 °C overnight (heating ramp of 2 °C min^{−1}). The specific surface area, S_{BET} , and total pore volume, V_{T} , were calculated from the isotherms. The pore size distributions were calculated by using the density functional theory (DFT) approach; the micropore volume was also evaluated by the DR method [26]. The Raman spectra were acquired with a Renishaw Raman instrument (InVia Raman Microscope), equipped with a Leica microscope. Spectra were obtained by excitation with green laser light (532 nm) in the range between 1000 and 2000 cm^{−1}. Fitting of the spectra was performed with the help of the Peakfit v. 4.11 software package. The chemical state and compositions of activated carbon aerogels were analyzed by using an X-ray Photoelectron Spectrometer (XPS, SPECS Phoebos 150MCD) with Al K source and a chamber

pressure of 4×10^{-9} mbar. Powdered samples were deposited as thin film samples on a holder and subjected to high vacuum overnight. Binding energies were referenced to the C 1s line of the adventitious carbon located at 284.6 eV. The deconvolution of the spectra was performed using the Casa XPS software.

2.3 Electrochemical response

Electrochemical measurements were performed in three-electrode SwagelokTM type cells. The working electrode consisted of a mixture of active material (70 %), Superior graphite (20 %), and PVDF binder (10 %). The powdered samples were slurried in *N*-methyl pyrrolidone to yield a paste which was subsequently spread on a 13-mm titanium disk. A Hg/Hg₂SO₄ and a platinum wire were, respectively, used as reference and counter electrode. The electrodes were dried at 70 °C overnight. The electrode was cooled and impregnated with the electrolyte solution before being assembled into the cell. The electrolyte solutions were prepared by dissolving NaNO₃ and Na₂HPO₄/NaH₂PO₄ in deionized water at 0.1 M. The use of a Na₂HPO₄/NaH₂PO₄ was intended to keep pH at the value of pH 7. The electrochemical measurements were controlled with a Biologic VMP multichannel potentiostat. Cyclic voltammetry experiments were conducted between −0.5 and +0.5 V versus the reference electrode for several sweep rates ranging from 0.5 to 10 mV s^{−1}. The capacitance of each electrode was calculated from the voltammograms using the relationship $C = I / (v \cdot m)$, where I (mA) is the average current in the applied potential window, v is the applied sweep rate in mV s^{−1}, and m is the mass of the electrode (normalized capacitance per unit mass of electrode). Chronocoulometric curves were performed by inducing a potentiostatic pulse of 300 mV versus Hg/Hg₂SO₄ for 120 s and recording the transient current.

Electrochemical impedance spectroscopy (EIS) was a helpful technique to analyze the kinetic response of the electrosorption reaction. These measurements were recorded in an Autolab PGSTAT12 system, using an AC voltage signal of 5 mV vs equilibrium potential (i.e., open circuit potential, which ranged from 0.4 to 0.6 V vs reference electrode), over the frequency range 25 kHz to 10 mHz at the equilibrium potential.

Capacitive deionization experiments were developed by using two monolithic aerogel electrodes previously polished to achieve a flat surface ensuring a good contact. The monoliths were previously washed in deionized water for 30 min and then were vacuum impregnated with the electrolyte. They were sandwiched between titanium current collectors using two Whatman glass GF/A fiber sheets as a separator. This symmetric cell was assembled in a bath cell containing 17 mL of the electrolyte under

continuous stirring to avoid mass transfer restrictions from the bulk solution. The deionization experiment was carried out by applying a potentiostatic pulse of 1.2 V for 150 min. Then, the discharge of the electrode was undergone at 0 V for the same period of time. A conductivity meter was used to monitor the change in the ionic concentration. Concentration values were calculated by previously recording a conductivity-concentration plot for each salt.

3 Results and discussion

3.1 Structural characterization of the aerogels

A series of carbon aerogels prepared using different R/C ratio were prepared and subjected to pyrolysis (series P) and activation in CO₂ (series A). Information about the structural properties of the synthesized materials was by XRD and Raman spectroscopy, shown in Figs. 1 and 2, respectively. The common features of XRD patterns are two broadened bands located at ca. 22.1 and ca. 44.5° (2θ), ascribable to the (002) and (100) reflections, respectively, both characteristic of disordered carbons. However, the reflection at 44.5° was rather marked and well-defined, indicating that despite the low structural ordering of the aerogels, there is an important contribution of domains of a graphitic structure. This is an unusual characteristic of nanoporous carbon materials synthesized at low temperatures. The first-order Raman spectra of the disordered carbons exhibited two highly broadened and overlapped bands in the region between 1000 and 2000 cm^{−1}. The parameters obtained from deconvolution of the spectra are compiled in Table 1. According to the literature, G band at ca. 1580 cm^{−1} is ascribed to a Raman-allowed *E*_{2g} resulting from to ‘in plane’ displacement of carbon atoms strongly coupled in the hexagonal sheets [27, 28]. A second maximum is observed at ca. 1350 cm^{−1} and named as ‘disorder-induced’ or D1 mode. It is commonly ascribed to the lack of a long range translation symmetry what breaks the k-momentum conservation rule [29]. An asymmetry of the G band is observed and resolved by adding a D2 lorentzian curve to the spectrum fitting [30]. The D2 band is usually ascribed to a lattice vibration involving graphene layers which are not directly sandwiched between two other graphene layers [31]. An additional Gaussian component was added at ca. 1495 cm^{−1}, designated as D3 band and correlated to amorphous sp²-bonded forms of carbon. Particularly, disordered carbons located at interstitial defects [32]. The peak at ca. 1310 cm^{−1} exhibits a shoulder at ca. 1160 cm^{−1}, commonly named as D4 [33], attributed to sp²–sp³ bonds or C–C and C=C stretching vibrations of polyene-like structures in Raman spectra of flame soot.

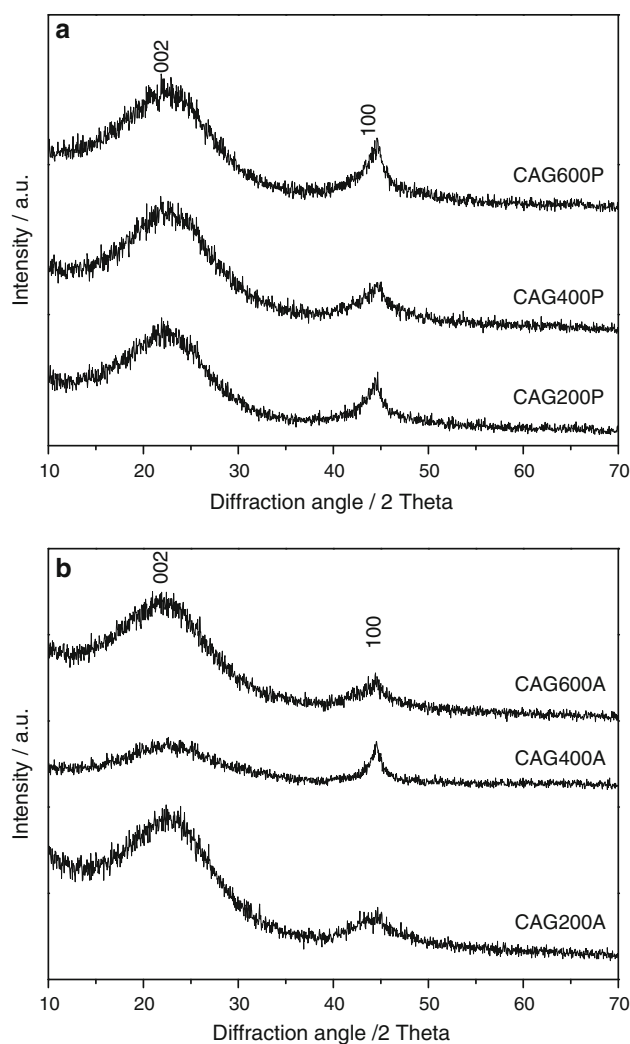


Fig. 1 X-ray diffraction patterns of **a** pyrolyzed and **b** activated aerogels. Diffractograms have been shifted for clarity

The lowest χ^2 values were achieved for the fitting of G and D2 signals to Lorentzian shapes and D1, D2, and D3 to Gaussian shapes. Table 1 clearly shows that widths of D1 and G bands are lower for the activated than for pyrolyzed aerogels. Moreover, the D1/G band intensity ratio also decreased upon activation of the samples, particularly for $R/C = 400$. In addition, a non negligible decrease in the I_{D1}/I_G ratio is observed when the R/C value increased in both activated and pyrolyzed aerogels. These trends indicate a dependence of the structure order with the R/C ratio, suggesting that high contents of resorcinol favor the formation of slightly more ordered carbon structures.

A semi-quantitative measurement of the functional groups attached to the aerogel surface can be determined by thermogravimetric measurements in Ar atmosphere (Fig. 3). Besides the mass loss below 200 °C due to the moisture retained in the pore network or the samples, a

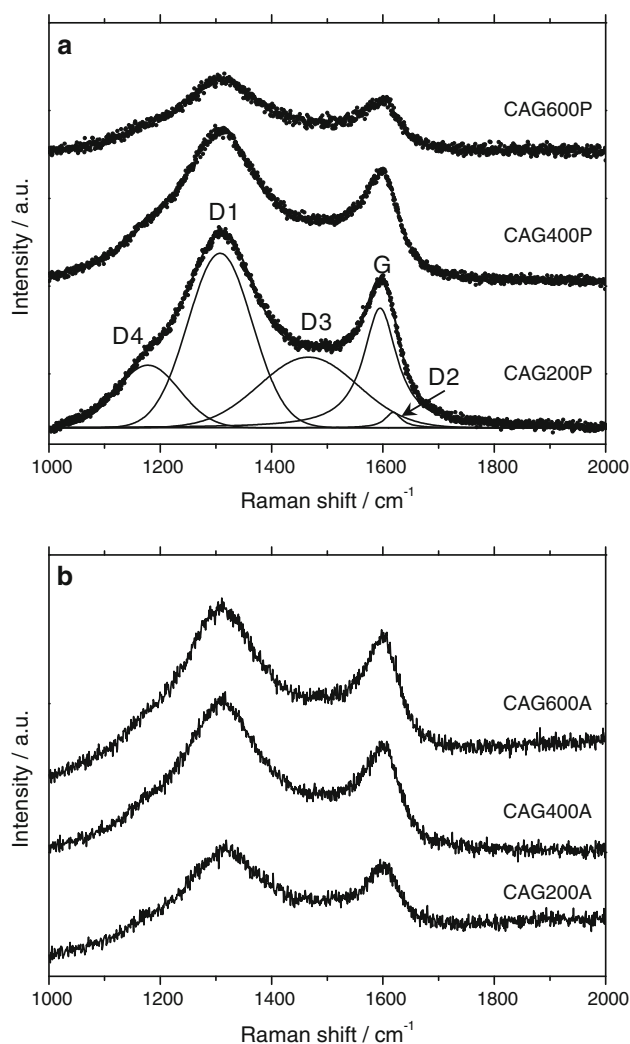


Fig. 2 Raman spectra of **a** pyrolyzed and **b** activated aerogels. Spectra have been shifted for clarity

Table 1 Raman shift and width values for the D1 and G bands calculated from the deconvoluted spectra

R/C	I_{D1}/I_G	D1 shift (cm ⁻¹)	G shift (cm ⁻¹)	D1 FWHM (cm ⁻¹)	G FWHM (cm ⁻¹)
Pyrolyzed					
200	2.67	1309.27	1594.15	153.74	68.97
400	2.53	1309.19	1594.00	148.18	66.64
600	2.28	1313.15	1597.04	138.61	65.54
Activated					
200	2.63	1317.53	1597.85	146.29	66.37
400	2.38	1312.19	1592.99	136.81	66.07
600	2.27	1312.19	1592.97	133.61	62.95

slight loss between 200 and 400 °C is observed for the pyrolyzed aerogel, indicating the presence of volatiles remaining in the sample. Above 700 °C, the activated

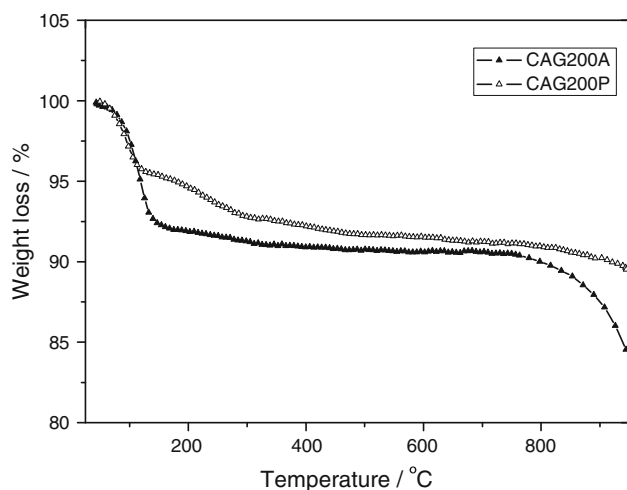


Fig. 3 Thermogravimetric curves of pyrolyzed and activated CAG200 aerogels

sample showed a non negligible weight loss likely due to the decomposition of surface groups incorporated during the activation.

The functionalization of the activated gels was further explored by recording the XPS spectra at the C1s and O1s levels (Fig. 4). The contribution of oxygen linked to carbon was found in the C1s spectra as C–O (285.6 ± 0.2 eV), C=O (287 ± 0.1 eV), and O=C–O (288.7 ± 0.3 eV) (Fig. 4a, c, e) [34]. The overall contribution of the oxygenated groups increased mainly for CAG200A. This result can be correlated to the larger surface area of the latter sample. The relative contribution of the C–O signal increased from 25.1 % for CAG600A to 35.1 % for CAG200A. Likewise, the contribution of C=O groups to the spectrum profiles increased when the R/C ratio decreased. This tendency was evidenced by the O1s spectra (Fig. 4b, d, f). These spectra are decomposed in two components at (532.1 ± 0.4 eV) and (533.5 ± 0.4 eV), attributed to C–O and C=O groups. The relative contribution of the single bond C–O groups progressively decreased from 54.2 % for CAG600A to 36.6 % for CAG200A, while an opposite tendency was observed for the signal of C=O. Otherwise, the contribution of O=C–O groups in the C1s spectra slightly decreased for CAG200A and CAG400A. The removal efficiency of inorganic salts has been directly correlated to the abundance of functionalized groups at the surface of carbon aerogels as a result of the improvement of the ion adsorption at the electric double layer and the electron transfer by Faradaic reaction [35].

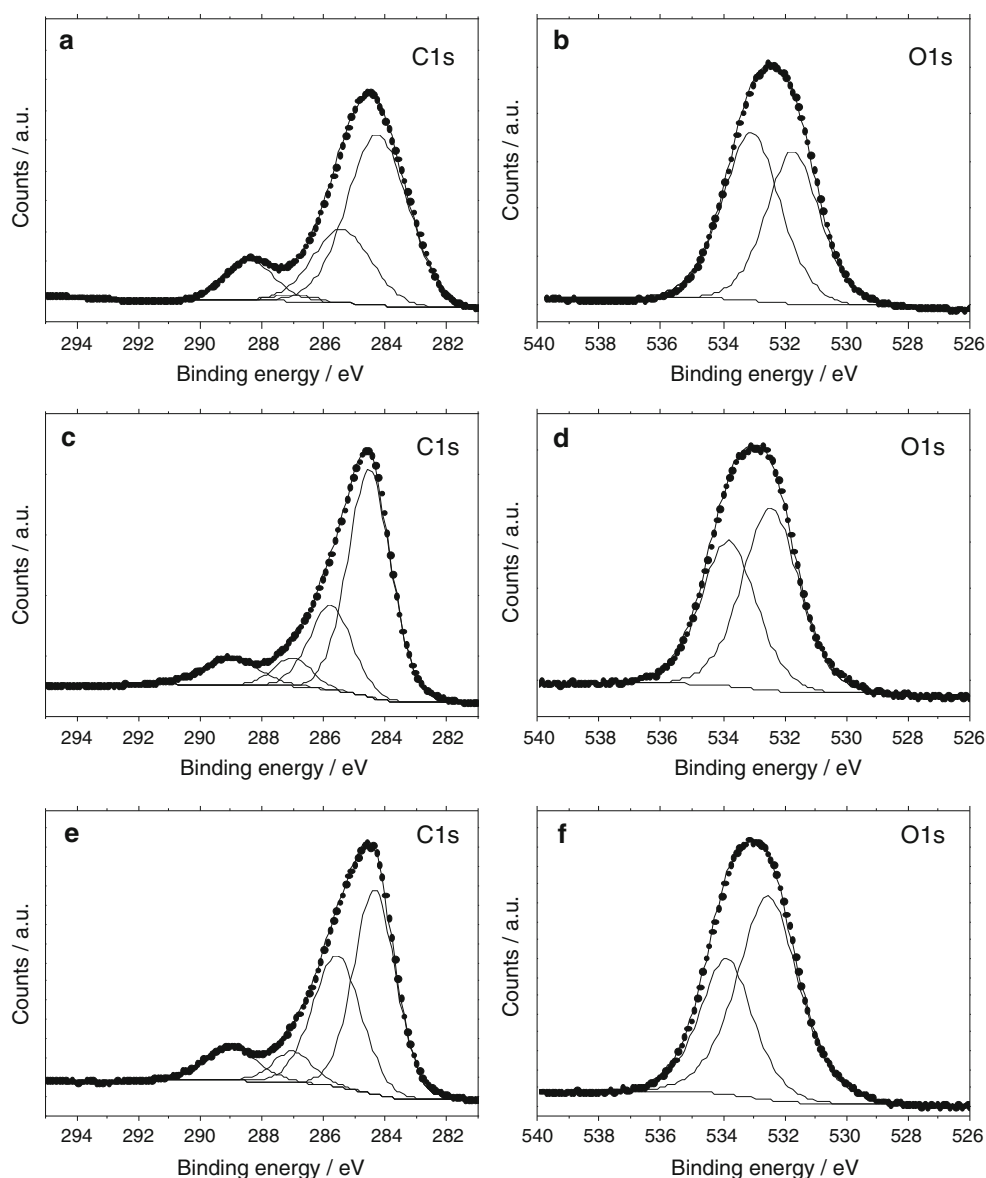
3.2 Textural characterization of the aerogels

The analysis of the textural properties of pyrolyzed and activated aerogels was performed by recording the nitrogen

adsorption isotherms at -196 °C (Fig. 5). All the isotherms (with the exception of CAG600A) can be classified as type IV according to BDDT classification, regardless the R/C ratio or the final thermal treatment (pyrolysis or activation). Samples displayed large adsorbed volumes at relative pressures below 0.2, indicating the presence of microporosity. Additionally, characteristic hysteresis loops above relative pressures p/p_0 0.6 were also obtained, indicating the presence of large (meso)pores. A large hysteresis loop (type H2) was observed for sample CAG200, attributed to samples with large pores presenting kinetic constrictions (i.e., ink-bottle shaped mesopores) [26]. In contrast, samples CAG400 and CAG600 showed smaller hysteresis loops shifted toward relative pressure close to unity. This indicates that very high R/C ratios favor the enlargement of mesopores; however, given the lower pore volumes corresponding to the hysteresis loop, it seems that there also occurs a slight collapse of the mesoporous structure for high R/C values.

The corresponding BET surface areas and additional porosity parameters are summarized in Table 2. For the non-activated aerogels, similar surface area values were obtained regardless the R/C ratio, with values close to $700 \text{ m}^2 \text{ g}^{-1}$. This is in good agreement with the fact that their isotherms overlap at relative pressures below 0.2–0.3 and the micropore volumes calculated from DR equation for the three aerogels (Table 2). Total pore volumes monotonically increased as the R/C ratio decreased; indicating that low R/C ratio results in a fast polycondensation favoring the formation of micro and mesopores. Contrarily, high R/C values yield large macropores formed by large clusters with a highly cross-linked structure [36]. On the other hand, the activation process induced a notorious increase in the surface area and micropore volume in all the samples, with some differences depending on the R/C ratio of the aerogels. For CAG200A (lowest R/C), the activation does not seem to strongly affect the mesoporosity, since the mesopore volume increased slightly but the hysteresis loop remained unchanged in position and shape. In the case of CAG400A, the development of microporosity upon activation is accompanied with a small increase in the mesopore volume, although the hysteresis loop shifts slightly toward lower relative pressures, indicating the presence of mesopores of smaller sizes. Finally, the activation provoked a clear change in the isotherm shape (type I after activation) for the sample with the highest R/C ratio, indicating either the collapse of the large pores or the formation of larger macropores, which size cannot be determined by N_2 adsorption at -196 °C. The pore size distribution displayed in Fig. 5 confirmed these observations, and revealed a direct relationship between the average pore size and the R/C ratio. High R/C ratios favor the formation of large pores, whereas a monodispersed pore

Fig. 4 XPS spectra at the C1s and O1s core levels of **a**, **b** CAG600A, **c**, **d** CAG400A, and **e**, **f** CAG200A



size distribution in the mesopore range was obtained for R/C of 200, with an average pore size of ca. 14 nm. These results agree with early reports on the porosity of carbon aerogels prepared with various R/C ratios [37, 38]. Summarizing, we have synthesized a series of carbon aerogels that exhibit a wide variety of porous features within the micro/mesopore range, which will undoubtedly influence upon their capacitive properties for the electro-assisted removal of ions [39].

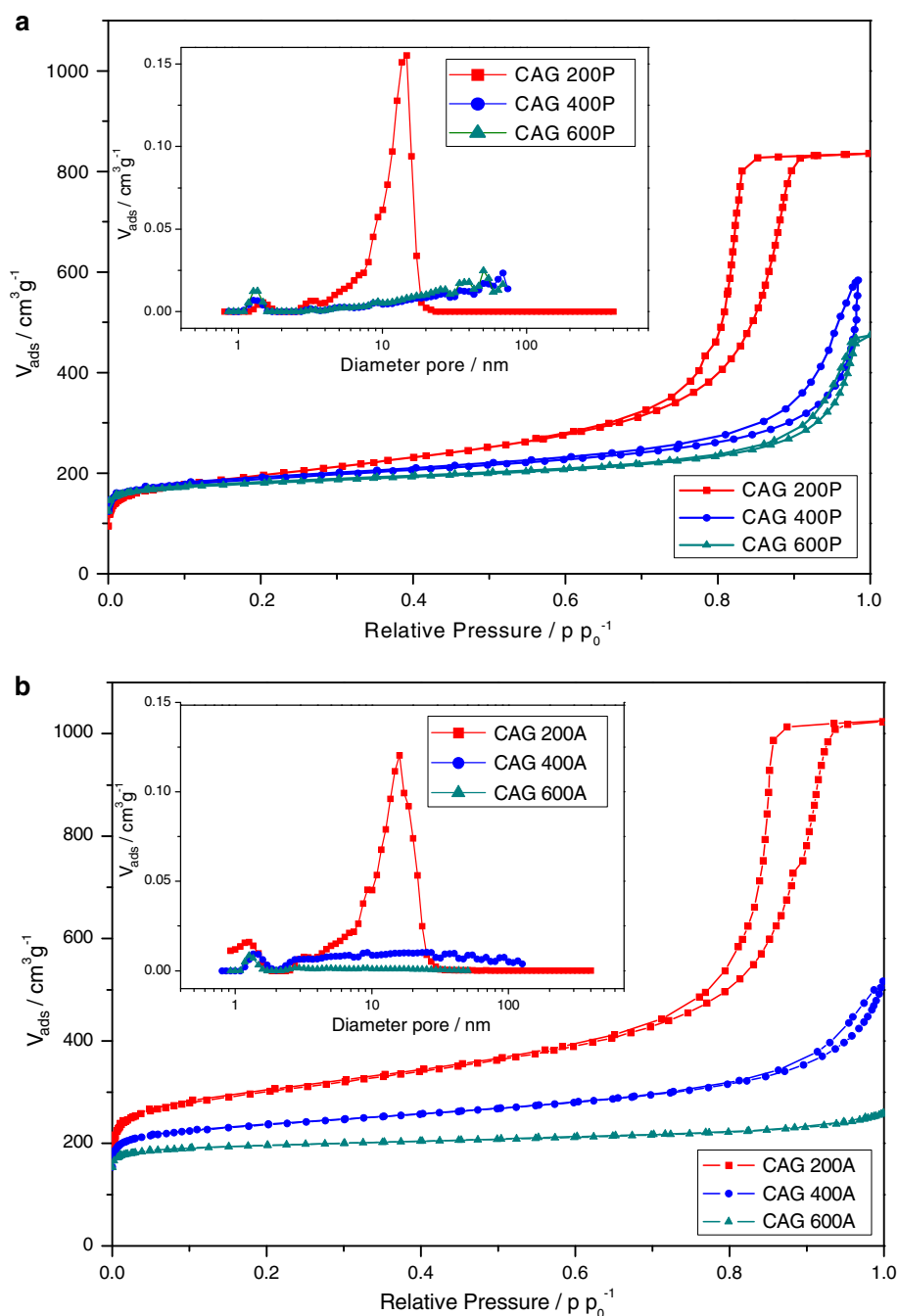
3.3 Electrochemical performance of the carbon aerogels

Cyclic voltammograms of pyrolyzed and activated aerogels were recorded in 0.1 M sodium nitrate and phosphate, respectively. Figure 6 shows the voltammograms recorded

at 0.5 mV s^{-1} in three-electrode cells. The profiles are characterized by a nearly rectangular loop expected for a pure capacitive behavior when ions are effectively electroadsorbed within the electric double layer at the electrode surface [40]. An anodic current increase likely related to pseudo-faradaic reactions was observed at potentials above +200 mV versus $\text{Hg}/\text{Hg}_2\text{SO}_4$ in some of the experiments, particularly for those samples exhibiting high surface areas. This effect has been correlated to side reaction including the electrolyte decomposition [40, 41]. It was more clearly detected in the voltammograms recorded in sodium phosphate solution.

The capacitance values of the pyrolyzed aerogels in NaNO_3 electrolyte varied as follows: CAG400P (46 F g^{-1}) < CAG600P (50 F g^{-1}) < CAG200P (91 F g^{-1}). The activation induced an increase in the

Fig. 5 N_2 adsorption isotherms at 77 K of the **a** pyrolyzed and **b** activated aerogels. *Inset* Pore size distribution plots



capacitance in all samples with the following trend: CAG600A (55 F g^{-1}) < CAG400A (71 F g^{-1}) < CAG200A (125 F g^{-1}). Interestingly, there is no clear correlation with the surface area or micropore volume of the aerogels (Table 2); instead, the desalting capacity seems to be related to the mesoporosity, pointing out the outstanding role of the accessibility of the ions to the inner porosity of the carbon electrodes (Supplementary info). For the sake of comparison, the capacitance values recorded for the adsorption of 0.1 M solution of NaCl were 79 and

110 F g^{-1} for CAG200P and CAG200A, respectively. Recently, capacitance values of 53.50 and 73.13 F g^{-1} were, respectively, found for activated carbons [42]. These values are close to those recorded for CAG200A in the same rate (61.5 F g^{-1}) evidencing the validity of our approach. The highest adsorption of NO_3^- anions has also been reported for ordered mesoporous carbon and hierarchical porous carbon and attributed to the balance between hydrated radius and valence providing stronger electrostatic force [43].

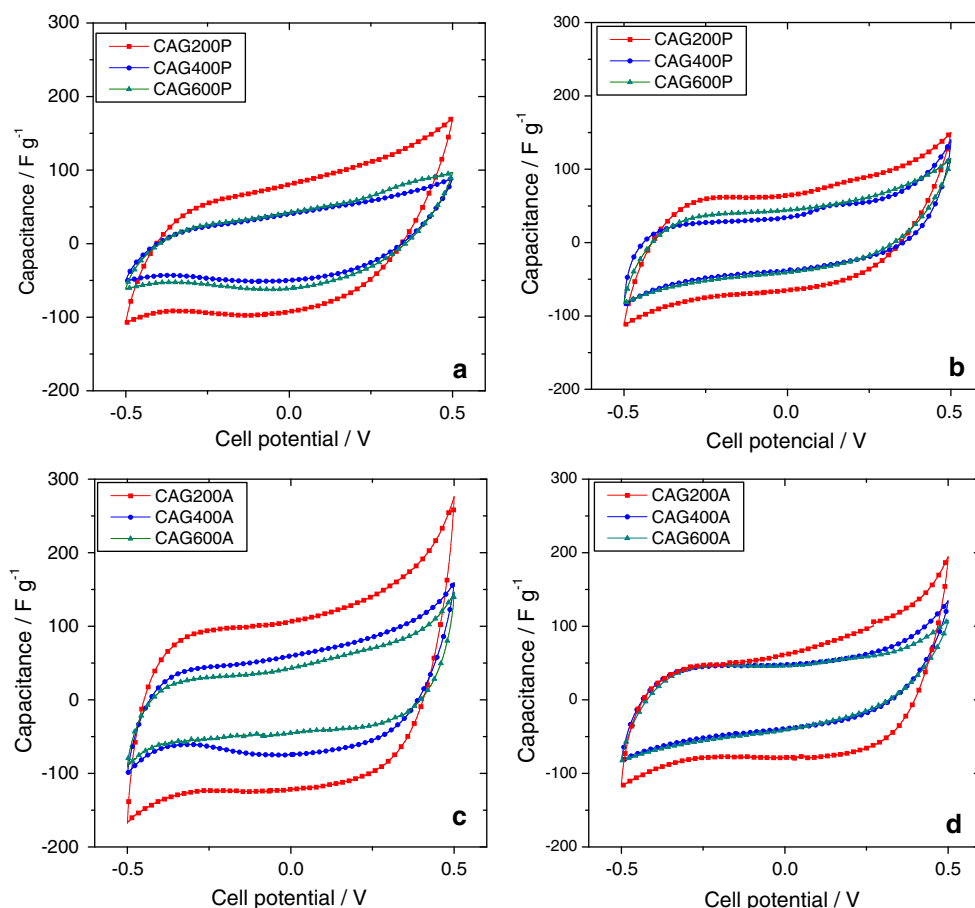
Table 2 BET surface area and pore volume values derived from the nitrogen isotherms measured for the aerogel samples

Pyrolyzed	CAG 200P	CAG 400P	CAG 600P
$S_{\text{BET}}/\text{m}^2 \text{ g}^{-1}$	712	718	701
$V_{\text{MICRO}}^{\text{a}}/\text{cm}^3 \text{ g}^{-1}$	0.27	0.28	0.27
$V_{\text{MESO}}/\text{cm}^3 \text{ g}^{-1}$	1.02	0.24	0.37
$V_{\text{TOTAL}}^{\text{b}}/\text{cm}^3 \text{ g}^{-1}$	1.29	0.91	0.72
Activated	CAG 200A	CAG 400A	CAG 600A
$S_{\text{BET}}/\text{m}^2 \text{ g}^{-1}$	1123	908	781
$V_{\text{MICRO}}^{\text{a}}/\text{cm}^3 \text{ g}^{-1}$	0.41	0.34	0.30
$V_{\text{MESO}}/\text{cm}^3 \text{ g}^{-1}$	1.15	0.34	0.04
$V_{\text{TOTAL}}^{\text{b}}/\text{cm}^3 \text{ g}^{-1}$	1.58	0.74	0.39

^a Evaluated from DR equation^b Evaluated at $p/p_0 \sim 0.99$

Compared to nitrate salt (Fig. 6b), capacitance values were similar in phosphate electrolyte for CAG400P (50 F g⁻¹) and CAG600P (55 F g⁻¹), with a significant decrease in the value obtained for CAG200P (78 F g⁻¹).

Previous reports have emphasized that the electrosorption procedure is influenced by both hydrated radius and the valence of the salt ions [44]. Therefore, we attribute this result to the large ionic size of phosphate anions [8]. Thus, it seems that the large pores in CAG400P and CAG600P would favor the adsorption of large phosphate anions, whereas the mesopores in CAG200P would not be large enough to suitably accommodate these ions. This is clearly seen also in the activated series; even though capacitance values of the activated samples are higher than those of the pyrolyzed ones—CAG400A (61 F g⁻¹), CAG600A (56 F g⁻¹), and CAG200A (82 F g⁻¹)—the effect was less pronounced than in the case of nitrates. These results point out to the lowest R/C ratio and activation as beneficial factors to provide enhanced capacitive performance for nitrate and phosphate adsorption. The high capacitance values recorded for activated samples can be correlated to the inherent decrease of density when amorphous carbon occupying inner pores is released by thermal activation. This fact is also supported by the fact that the range of size of mesopores found in CAG200P is not wide enough to

**Fig. 6** Cyclic voltammograms of **a, b** pyrolyzed and **c, d** activated carbon aerogels recorded at 0.5 mV s⁻¹ in 0.1 M electrolyte solutions of **a, c** sodium nitrate and **b, d** sodium phosphate

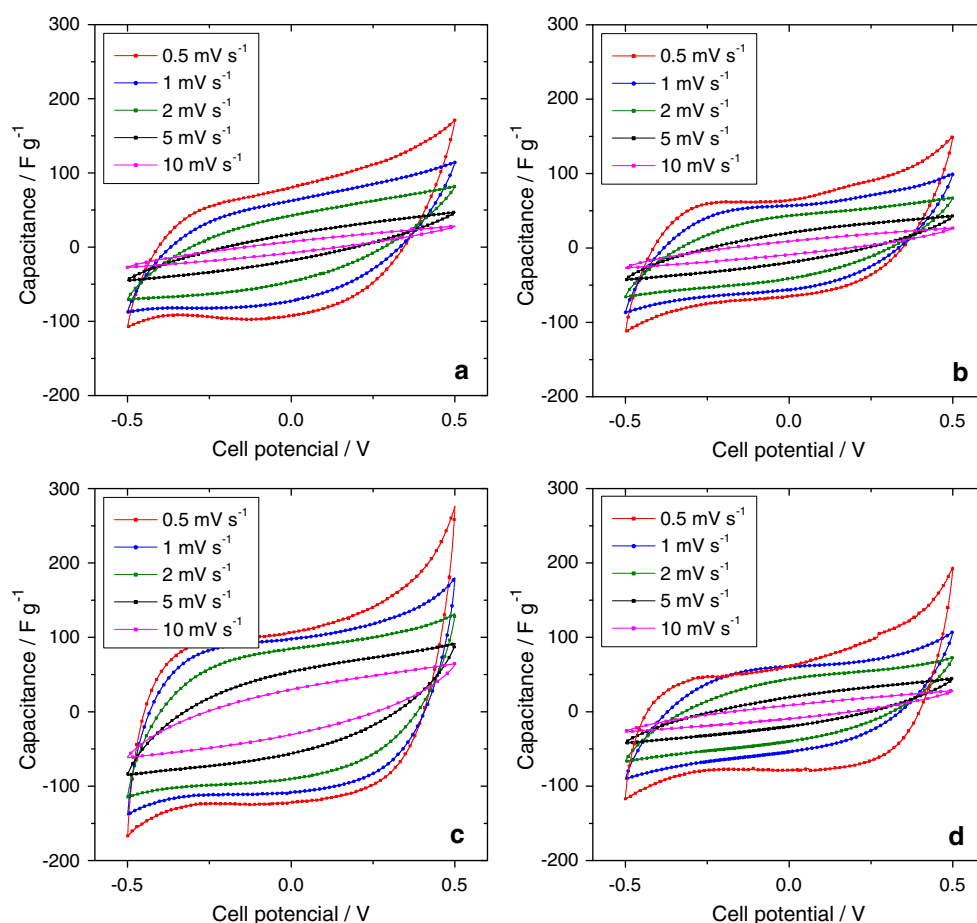


Fig. 7 Cyclic voltammograms of **a, b** CAG200P and **c, d** CAG200A carbon aerogels in 0.1 M electrolyte solutions of **a, c** sodium nitrate and **b, d** sodium phosphate

accommodate the large phosphate ions, inferring that micropores do not effectively contribute to the adsorption of these anions (Supplementary info). Figure 7 shows the cyclic voltammograms recorded for CAG200A at several scan rates in the presence of solutions of nitrate and phosphate anions. On increasing the scan rate, the typical rectangular shape is distorted becoming a leaf-like shape, and a decrease in the capacitance is detected. The rate-dependent behavior results from the limited time to transport the salt ions and diffuse into the inner pores of the bulk phase. As a consequence, the accessible surface area for ion adsorption is reduced [43]. An extended cycling of a cell assembled with a CAG200A electrode, immersed in 0.1 M solution of NaNO_3 , demonstrated to be stable for a long-term cycling (Fig. 8).

The ohmic resistances for ionic migration into the pores at high rates have an influence on the formation of the electric double layer. Thus, the evaluation of the kinetic behavior is needed for a full electrochemical characterization of these electrodes. The kinetic response of pyrolyzed and activated carbon aerogel was analyzed by the

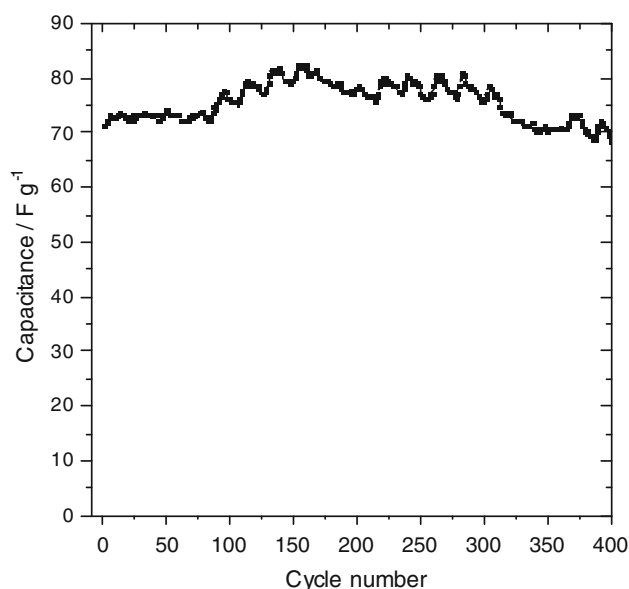
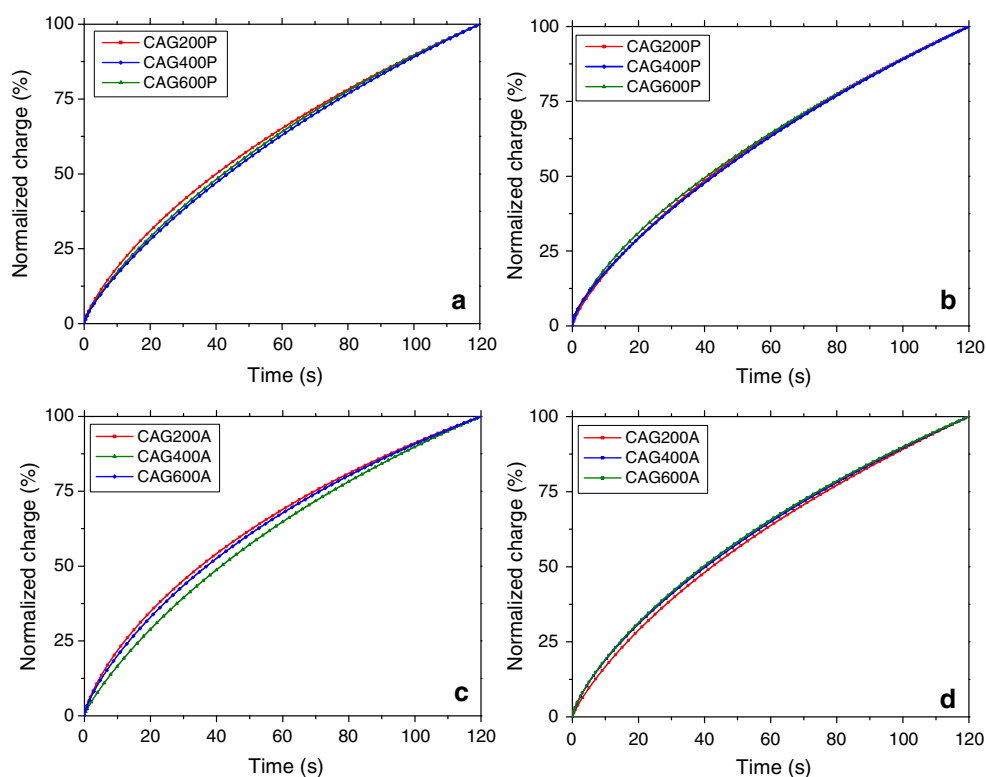


Fig. 8 Extended cycling voltammetry of CAG200A in a 0.1 M NaNO_3 solution. Scan rate: 2 mV s^{-1}

Fig. 9 Normalized chronocoulometric curves of pyrolyzed (**a, b**) and activated (**c, d**) carbon aerogels in 0.1 M electrolyte solutions of **a, c** sodium nitrate and **b, d** sodium phosphate



chronocoulometric relaxation after subjecting the cell to a potential step (Fig. 9). For the sake of comparison, charge values have been normalized to the maximum accumulated charge at the end of the experiment of each of the studied aerogels. A first-order kinetics is obtained for most of the pulse time comprising at least the seventy percent of the total accumulated charge. By applying the following equation to the charge transient curve, the time constants ($\tau = R_e C_{sp}$) can be calculated [37]:

$$-\ln\left(1 - \frac{Q}{Q_0}\right) = \frac{t}{R_e C_{sp}} \quad (1)$$

where Q_0 is the electrode's charge at the equilibrium and t is the time of the potential step. R_e and C_{sp} are the resistance and specific capacitance of the electrode, respectively. The values are compiled in Table 3. Regarding separately the four rows of values corresponding to the electrosorption in pyrolyzed and activated, the lowest time constants were recorded for CAG200 aerogels. It evidences the beneficial effect of the large mesoporous volume recorded for these samples. Otherwise, the adsorption of sodium nitrate is less kinetically impeded for CAG200 and CAG400 as inferred from the lower values recorded in these experiments. In general, the activation of the carbon aerogels brought about a decrease in the time constant for both electrolytes. It can be attributed to the pore opening effect exerted by the thermal reaction with CO_2 . Nevertheless, the decrease observed for the

Table 3 Time constants (τ) calculated from the chronocoulometric curves

	CAG 200 (τ/s)	CAG 400 (τ/s)	CAG 600 (τ/s)
Sodium nitrate			
Pyrolyzed	61.8	66.5	64.5
Activated	54.5	57.4	61.9
Sodium phosphate			
Pyrolyzed	63.9	67.0	64.2
Activated	63.7	62.6	61.4

adsorption of sodium phosphate on activated CAG200A was lower than for the other aerogels.

Impedance spectroscopy is a valuable tool to determine the internal electrode resistance to the ion migration at the carbon aerogel. The Nyquist plots for both pyrolyzed and activated aerogels immersed in the electrolyte solutions are shown in Fig. 10. These plots have been fitted to the equivalent circuit included in Fig. 10b. R_{elec} is the solution resistance, R_{pol} is the polarization impedance, W is the Warburg impedance, and CPE is a constant phase element is used to overcome the non-ideal behavior of the electrode. The high-frequency response is ascribable to the bulk resistance of the solution (R_{el}), whose contribution to the cell resistance was negligible. The analysis of this domain was not regarded because of the negligible contribution. The resistance to ion migration through the pore

Fig. 10 Nyquist plots from impedance spectra recorded for pyrolyzed (**a, b**) and activated (**c, d**) carbon aerogels in 0.1 M electrolyte solutions of **a, c** sodium nitrate and **b, d** sodium phosphate. *Inset* Equivalent circuit applied to the fitting of the impedance spectra

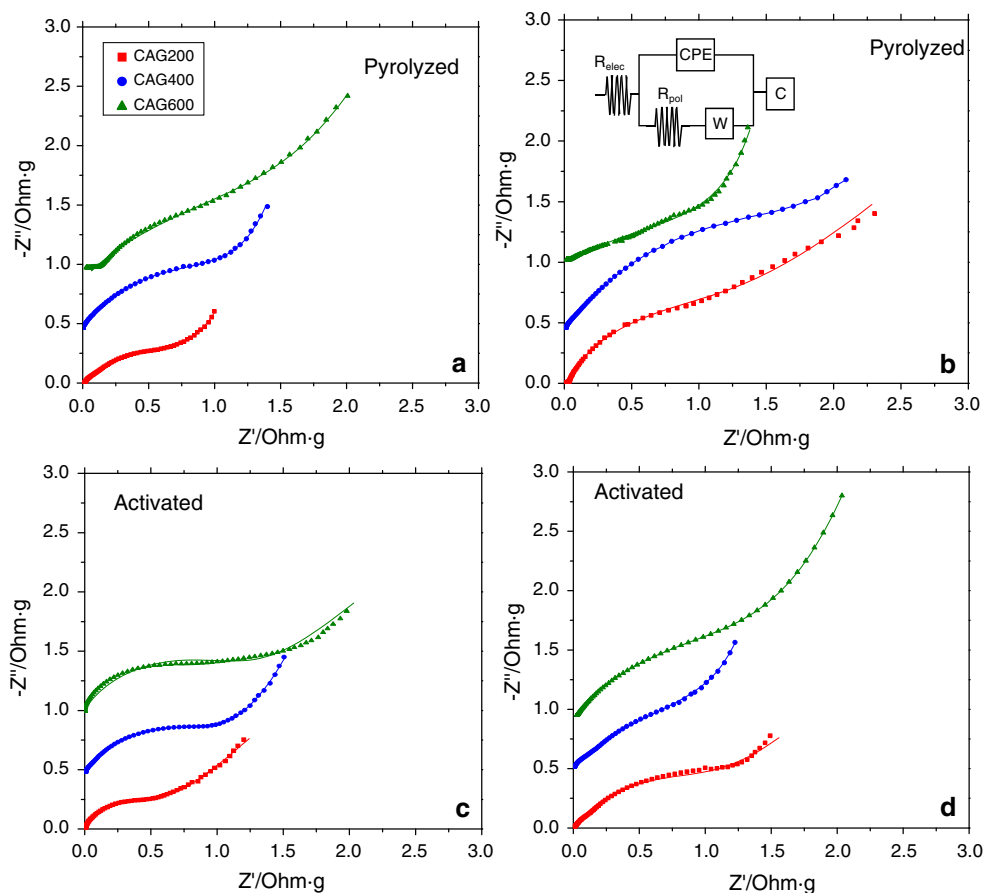


Table 4 Electrical resistances (R_{pol}) as derived from the fitted impedance spectra of the carbon aerogel electrodes

	CAG 200 ($R_{pol}/\Omega \times g$)	CAG 400 ($R_{pol}/\Omega \times g$)	CAG 600 ($R_{pol}/\Omega \times g$)
Sodium nitrate			
Pyrolyzed	0.95	1.35	2.34
Activated	0.60	0.84	1.44
Sodium phosphate			
Pyrolyzed	1.36	2.68	2.54
Activated	1.67	1.66	1.78

structure is determined from the real impedance of the semicircle located at intermediate frequencies (R_{pol}) [45, 46]. The resistance values calculated for the aerogel electrodes (Table 4) showed a similar sequence to that observed for the time constants calculated from the chronocoulometric curves.

As seen, R_{pol} values corresponding to the electrosorption of sodium nitrate decreased with the activation of the samples, suggesting that the pore widening occurring during the activation reaction [4] facilitates the accessibility and thus the migration of ions. Resistance values were

higher for the adsorption of phosphates, as expected given the larger size of these ions. Interestingly, a high R_{pol} value was obtained for the adsorption of phosphates on activated CAG200A. Similar results were recently observed for a related aerogel prepared at $R/C = 100$, being attributed to the higher increase of micropore volume built after the activation reaction. It exerts a sieve effect that hinders the migration of large phosphate anions [47]. This result is in good agreement with the slow relaxation observed for this aerogel (Table 3).

Comparatively, the electrochemical characterization of the series of carbon aerogel electrodes indicates the better performance of CAG200A over the rest of the materials. It seems that the existence of a well-developed unimodal mesoporous structure in CAG200A is a crucial factor determining the fast response and high capacitance for the electrosorption of nitrate and phosphate anions [48].

Based on its better performance in sodium nitrate, CAG200A electrode was selected to evaluate the effect of the electrolyte concentration and the applied voltage on the electrosorption capacity. Figure 11a reveals the enhanced and fast desalting capacity with the electrolyte concentration, with 96 % of the maximum capacity after 100 min in 0.1 M NaNO_3 , as opposed to only 75 % when a 0.025 M

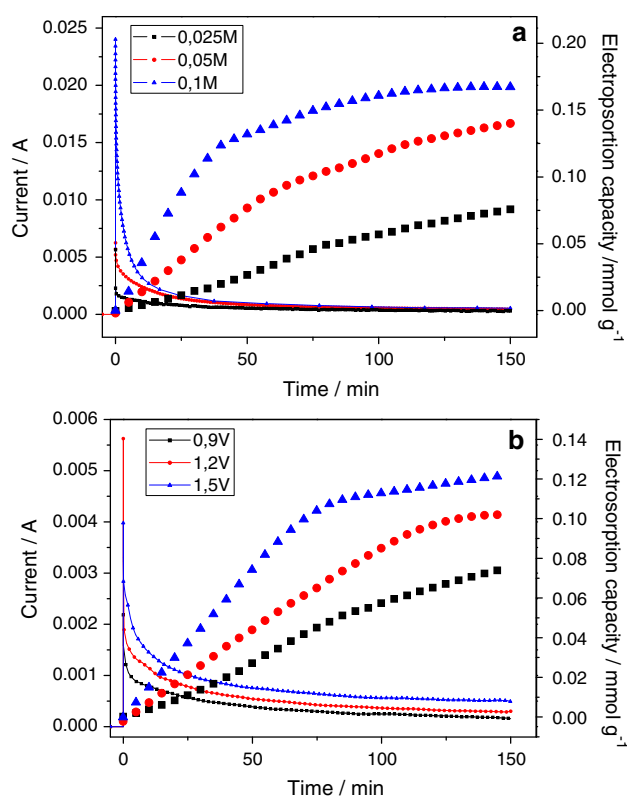


Fig. 11 Electrosorption capacity of sodium nitrate and relaxation current curves for the activated CAG200A carbon aerogel at different **a** concentrations of electrolyte by applying 1.2 V and **b** applied voltages in 0.025 M electrolyte solution

solution was employed. This result shows the suitability of the CAG200A electrode to efficiently remove ionic species from concentrated electrolytes. The effect of the applied voltage was also evaluated in 0.025 M NaNO_3 , in order to optimize the electrosorption properties of CAG200A under these conditions (Fig. 11b). The electrosorption capacity increased to 0.10 and 0.12 mmol g^{-1} for applied voltages of 1.2 and 1.5 V, respectively. Despite the higher desalting capacity at 1.5 V, a high residual relaxation current was recorded after the charge period. This can be indicative of certain irreversibility, for which 1.2 V was chosen for further experiments on the cycleability of the electrodes.

Figure 12 shows the performance of symmetric cells using pyrolyzed and activated CAG200 aerogel as electrodes on consecutive charge/discharge cycles in 0.1 M NaNO_3 and Na_3PO_4 . As expected based on the electrochemical characterization of the electrodes on the 3-electrode cell, higher deionization capacities were obtained for the activated aerogel electrode compared to the pyrolyzed one. Most importantly, this trend was maintained after several cycles, indicating that the electrodes are stable at the high applied potentials in both electrolytes. The electrosorption capacity was higher for sodium nitrate (0.17 mmol g^{-1}) than for sodium phosphate

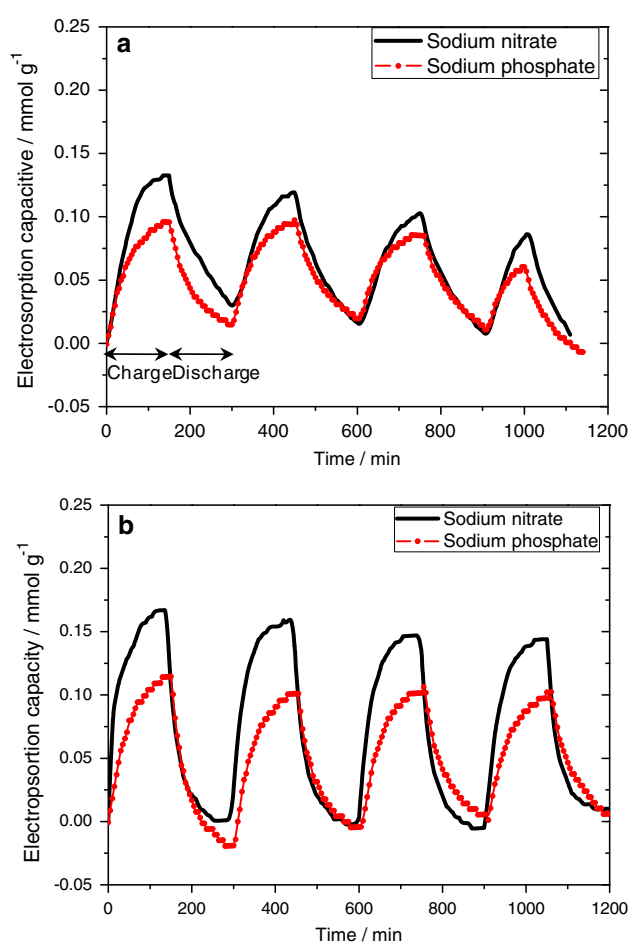


Fig. 12 Electrosorption capacity of 0.1 M solutions of sodium nitrate and phosphate applying 1.2 V on **a** pyrolyzed and **b** activated CAG200 carbon aerogel

(0.11 mmol g^{-1}), which is also in good agreement with the capacitance values recorded in the 3-electrode cells for this sample (Fig. 5). These values are well above those reported for the adsorption of nitrate on carbon cloth [49]. The discharge of nitrate anions was more efficient after activation of the aerogel, revealing the beneficial effect of activation upon the nitrate electrosorption. This result agrees with the lower impedance and time constant observed for the sodium nitrate electrosorption in pyrolyzed CAG200.

4 Conclusions

Three carbon aerogels with varied R/C ratio were synthesized and subsequently activated under CO_2 in order to prepare electrode materials with different micro/mesopore structure. XRD patterns and Raman spectra showed that despite the low structural ordering of the aerogels, there is an important contribution of domains of a graphitic structure, very unusual for carbon aerogels nanoporous carbons

synthesized at low temperatures. Raman spectroscopy also showed a correlation between the structural ordering and the *R/C* ratio, with high resorcinol contents favoring the formation of more ordered carbon structures.

All the synthesized carbon aerogels presented a well-developed micro/mesoporous structure. Whereas all the pyrolyzed materials presented similar microporosity, regardless the *R/C* ratio, the formation of mesopores with a narrow size distribution is connected to low *R/C* values. In contrast, high *R/C* values yield large macropores resulting from large clusters with a highly cross-linked structure. Activation under CO₂ provoked an increase in the micro-pore volumes, accompanied by the enlargement of the mesopores—this effect being more significant for samples with *R/C* 400 and 600.

Cyclic voltammograms in various electrolytes showed large capacitance values for sample CAG200A, likely attributed to its enhanced surface area and pore volume, as well as an accessible pore structure that enables fast charge kinetics and ion migration for the electrosorption of both salts. The desalination experiments performed in both ionic solutions using pyrolyzed and activated CAG200A aerogel electrodes revealed an efficient electrosorption of ionic species on consecutive charge/discharge cycles, confirming the stability of the aerogel electrodes at the high applied potentials in both electrolytes.

Acknowledgments The authors are indebted to the MICINN (Contract IPT-2011-1450-310000 (ADECAR), and CTM2011/23378) for the financial support. We also thank the fruitful collaboration of Isolux Ingeniería, S.A., Fundación Imdea Energía and Proingesa.

References

- Porada S, Zhao R, van der Wal A, Presser V, Biesheuvel PM (2013) Review on the science and technology of water desalination by capacitive deionization. *Prog Mater Sci* 58:1388–1442
- Candelaria SL, Shao Y, Zhou W, Li X, Xiao J, Zhang JG, Wang Y, Liu J, Li J, Cao G (2012) Nanostructured carbon for energy storage and conversion. *Nano Energy* 1:195–220
- Oren Y (2008) Review on the science and technology of water desalination by capacitive deionization. *Desalination* 228:10–29
- Marsh H, Rodríguez-Reinoso F (2006) Activated carbon. Elsevier, Amsterdam
- Anderson MA, Cudero AL, Palma J (2010) Capacitive deionization as an electrochemical means of saving energy and delivering clean water. Comparison to present desalination practices: will it compete? *Electrochim Acta* 55:3845–3856
- Dehkhoda AM, Ellis N, Gyenge E (2014) Electrosorption on activated biochar: effect of thermo-chemical activation treatment on the electric double layer capacitance. *J Appl Electrochem* 44:141–157
- Peng Z, Zhang D, Shi L, Yan T, Yuan S, Li H, Gao R, Fang J (2011) Comparative electroadsorption study of mesoporous carbon electrodes with various pore structures. *J Phys Chem C* 115:17068–17076
- Ania CO, Pernak J, Stefaniak F, Raymundo-Pinero E, Beguin F (2009) Polarization-induced distortion of ions in the pores of carbon electrodes for electrochemical capacitors. *Carbon* 47:3158–3166
- Chmiola J, Largeot C, Taberna PL, Simon P, Gogotsi Y (2008) Desolvation of ions in subnanometer pores and its effect on capacitance and double layer theory. *Angew Chem* 47:1–5
- Zhang D, Yan T, Shi L, Peng Z, Wen X, Zhang J (2012) Enhanced capacitive deionization performance of graphene/carbon nanotube composites. *J Mater Chem* 22:14696–14704
- Liang P, Yuan L, Yang X, Zhou S, Huang X (2013) Coupling ion-exchangers with inexpensive activated carbon fiber electrodes to enhance the performance of capacitive deionization cells for domestic wastewater desalination. *Water Res* 47:2523–2530
- Seo SJ, Jeon H, Lee JK, Kim GY, Park D, Nojima H, Lee J, Moon SH (2010) Investigation on removal of hardness ions by capacitive deionization (CDI) for water softening applications. *Water Res* 44:2267–2275
- Porada S, Weinstein L, Dash R, van der Wal A, Bryjak M, Gogotsi Y, Biesheuvel PM (2012) Water desalination using capacitive deionization with microporous carbon electrodes. *ACS Appl Mater Interfaces* 4:1194–1199
- Punckt C, Pope MA, Liu J, Lin Y, Aksay IA (2010) Electrochemical performance of graphene as effected by electrode porosity and graphene functionalization electroanalysis. *Electroanalysis* 22:2834–2841
- Ban A, Schafer A, Wendt H (1998) Fundamentals of electrosorption on activated carbon for wastewater treatment of industrial effluents. *J Appl Electrochem* 157:602–615
- Tsouris C, Mayes R, Kiggans J, Sharma K, Yiaccoumi S, DePaoli D, Dai S (2011) Mesoporous carbon for capacitive deionization of saline water. *Environ Sci Technol* 45:10243–10249
- Xu LY, Shi ZG, Feng YQ (2008) Preparation of a carbon monolith with bimodal perfusion pores. *Microporous Mesoporous Mater* 115:618–623
- Wen X, Zhang D, Yan T, Wang H, Zhang J, Shi L (2013) Three-dimensional graphene-based hierarchically porous carbon composites prepared by a dual-template strategy for capacitive deionization. *J Mater Chem A* 1:12334–12344
- Wang H, Shi L, Yan T, Zhang J, Zhong Q, Zhang D (2014) Design of graphene-coated hollow mesoporous carbon spheres as high performance electrodes for capacitive deionization. *J Mater Chem A* 2:4739–4750
- Pekala RW, Farmer JC, Alviso CT, Tran TD, Mayer ST, Miller JM, Dunn B (1998) Carbon aerogels for electrochemical applications. *J Non Cryst Solids* 225:74–80
- Gross J, Scherer GW, Alviso CT, Pekala RW (1997) Elastic properties of crosslinked resorcinol-formaldehyde gels and aerogels. *J Non Cryst Solids* 211:132–142
- Hadas A, Sagiv B, Haruvy N (1999) Agricultural practices, soil fertility management modes and resultant nitrogen leaching rates under semi-arid conditions. *Agric Water Manag* 42:81–95
- Broséus R, Cigana J, Barbeau B, Daines-Martinez C, Suty H (2009) Removal of total dissolved solids, nitrates and ammonium ions from drinking water using charge-barrier capacitive deionization. *Desalination* 249:217–223
- Pekala RW (1989) Organic aerogels from the polycondensation of resorcinol with formaldehyde. *J Mater Sci* 24:3221–3227
- Haro M, Rasines G, Macías C, Ania CO (2011) Stability of a carbon gel electrode when used for the electro-assisted removal of ions from brackish water. *Carbon* 49:3723–3730
- Rouquerol F, Rouquerol J, Sing K (1999) Adsorption by powders and porous solids. Academic Press, London
- Tuinstra F, Koenig JL (1970) Raman spectrum of graphite. *J Chem Phys* 53:1126–1130
- Cuesta A, Dhamelincourt P, Laureyns J, Martinez-Alonso A, Tascon JMD (1994) Raman microprobe studies on carbon materials. *Carbon* 32:1523–1532

29. Jawhari T, Roid A, Casado J (1995) Raman spectroscopic characterization of some commercially available carbon black materials. *Carbon* 33:1561–1565
30. Sze SK, Siddique N, Sloan JJ, Escribano R (2001) Raman spectroscopic characterisation of carbonaceous aerosol. *Atmos Environ* 35:561–568
31. Dresselhaus MS, Dresselhaus G (1982) *Light-scattering in graphite-intercalation compounds*. Springer, Berlin
32. Rouzaud JN, Oberlin A, Beny-Bassez C (1983) Carbon-films-structure and microtexture (optical and electron-microscopy, raman-spectroscopy). *Thin Solid Films* 105:75–96
33. Dippel B, Jander H, Heintzenberg J (1999) NIR FT Raman spectroscopic study of flame soot. *Phys Chem Chem Phys* 1:4707–4712
34. Biniak S, Szymanski G, Siedlewski J, Swiatkowski A (1997) The characterization of activated carbons with oxygen and nitrogen surface groups. *Carbon* 35:1799–1810
35. Oh HJ, Lee JH, Ahn H-J, Jeong Y, Kim YJ, Chi CS (2006) Nanoporous activated carbon cloth for capacitive deionization of aqueous solution. *Thin Solid Films* 515:220–225
36. Tamon H, Ishizaka H, Araki T, Okazaki M (1998) Control of mesoporous structure of organic and carbon aerogels. *Carbon* 36:1257–1262
37. Job N, Thery A, Pirard R, Marien J, Kocon L, Rouzaud JN, Beguin F, Pirard JP (2005) Carbon aerogels, cryogels and xerogels: influence of the drying method on the textural properties of porous carbon materials. *Carbon* 43:2481–2494
38. Tamon H, Ishizaka H, Mikami M, Okazaki M (1997) Porous structure of organic and carbon aerogels synthesized by sol–gel polycondensation of resorcinol with formaldehyde. *Carbon* 35:791–796
39. Peng Z, Zhang D, Yana T, Zhang J, Shi L (2013) Three-dimensional micro/mesoporous carbon composites with carbon nanotube networks for capacitive deionization. *Appl Surf Sci* 282:965–973
40. Hsieh CT, Teng H (2002) Influence of oxygen treatment on electric double-layer capacitance of activated carbon fabrics. *Carbon* 40:667–674
41. Pröbstle H, Wiener M, Fricke J (2003) Carbon aerogels for electrochemical double layer capacitors. *J Porous Mater* 10:213–222
42. Huang W, Zhang Y, Bao S, Cruz R, Song S (2014) Desalination by capacitive deionization process using nitric acid-modified activated carbon as the electrodes. *Desalination* 340:67–72
43. Wen X, Zhang D, Shi L, Yan T, Wang H, Zhang J (2012) Three-dimensional hierarchical porous carbon with a bimodal pore arrangement for capacitive deionization. *J Mater Chem* 22:23835–23844
44. Peng Z, Zhang D, Shi L, Yan T (2012) High performance ordered mesoporous carbon/carbon nanotube composite electrodes for capacitive deionization. *J Mater Chem* 22:6603–6612
45. Noked M, Avraham E, Soffer A, Aurbach D (2009) The rate-determining step of electroadsorption processes into nanoporous carbon electrodes related to water desalination. *J Phys Chem C* 113:21319–21327
46. Miller JM, Dunn B (1999) Morphology and electrochemistry of ruthenium/carbon aerogel nanostructures. *Langmuir* 15:799–806
47. Zafra MC, Lavela P, Macías C, Rasines G, Tirado JL (2013) Electrosorption of environmental concerning anions on a highly porous carbon aerogel. *J Electroanal Chem* 708:80–86
48. Yang J, Zou L (2014) Using recyclable calcium citrate templates to prepare mesoporous carbons as electrodes for capacitive deionization. *Microporous Mesoporous Mater* 183:91–98
49. Afkhami A (2003) Adsorption and electrosorption of nitrate and nitrite on high-area carbon cloth: an approach to purification of water and waste-water samples. *Carbon* 41:1309–1328